GFZ
Helmholtz-Zentrum
POTSDAM

Originally published as:

Seismic Amplitude Ratio Analysis of the 2014–2015 Bárðarbunga-Holuhraun Dike Propagation and Eruption

Corentin Caudron[1,2,3,4] ![ID], Robert S. White[1] ![ID], Robert G. Green[1,5] ![ID], Jennifer Woods[1] ![ID], Thorbjörg Ágústsdóttir[1] ![ID], Clare Donaldson[1] ![ID], Tim Greenfield[1,6] ![ID], Eleonora Rivalta[5] ![ID], and Bryndís Brandsdóttir[7] ![ID]

[1]Department of Earth Sciences, Bullard Laboratories, University of Cambridge, Cambridge, UK, [2]Laboratoire de Volcanologie, G-Time, Département Géosciences Environnement Société, Université Libre de Bruxelles, Brussels, Belgium, [3]Seismology and Gravimetry Department, Royal Observatory of Belgium, Uccle, Belgium, [4]Department of Geology, Ghent University, Ghent, Belgium, [5]Helmholtz-Centre Potsdam - GFZ German Research Centre for Geosciences, Potsdam, Germany, [6]University of Southampton, Southampton, UK, [7]Institute of Earth Sciences, University of Iceland, Reykjavík, Iceland

Abstract Magma is transported in brittle rock through dikes and sills. This movement may be accompanied by the release of seismic energy that can be tracked from the Earth's surface. Locating dikes and deciphering their dynamics is therefore of prime importance in understanding and potentially forecasting volcanic eruptions. The Seismic Amplitude Ratio Analysis (SARA) method aims to track melt propagation using the amplitudes recorded across a seismic network without picking the arrival times of individual earthquake phases. This study validates this methodology by comparing SARA locations (filtered between 2 and 16 Hz) with the earthquake locations (same frequency band) recorded during the 2014–2015 Bárðarbunga-Holuhraun dike intrusion and eruption in Iceland. Integrating both approaches also provides the opportunity to investigate the spatiotemporal characteristics of magma migration during the dike intrusion and ensuing eruption. During the intrusion SARA locations correspond remarkably well to the locations of earthquakes. Several exceptions are, however, observed. (1) A low-frequency signal was possibly associated with a subglacial eruption on 23 August. (2) A systematic retreat of the seismicity was also observed to the back of each active segment during stalled phases and was associated with a larger spatial extent of the seismic energy source. This behavior may be controlled by the dike's shape and/or by dike inflation. (3) During the eruption SARA locations consistently focused at the eruptive site. (4) Tremor-rich signal close to ice cauldrons occurred on 3 September. This study demonstrates the power of the SARA methodology, provided robust site amplification; Quality Factors and seismic velocities are available.

Plain Language Summary Locating earthquakes usually implies picking phase arrivals (*P* and *S* waves). Another technique called Seismic Amplitude Ratio Analysis (SARA) was recently introduced to locate them only by using the amplitude recorded at different pairs of seismic stations. However, this technique was never proven to be true. This study shows that the earthquake locations derived by SARA compares remarkably well with the locations of 30,000 seismic events triggered when magma migrated in the Icelandic crust prior to the 2014–2015 Holuhraun eruption. But the results also provide new insight into the magma dynamics that led to the largest eruption of the last two centuries in Europe. We show that ground vibration was continuously triggered during the 2 week period preceding the eruption when magma forced its way toward the eruption site but also during the eruption itself. Several intriguing features were observed including low-frequency vibrations possibly associated with eruption below the ice, or large patches of seismic activity when the magma stopped propagating toward the eruption site. This methodology performs very well, provided some parameters are available, and allows to gain insights into the complex dynamics associated with magma movements.

1. Introduction

The 2014–2015 Holuhraun eruption in Iceland was the largest eruption of the last two centuries in Europe (Gudmundsson et al., 2016). During the 2 weeks preceding the long-lasting eruption (from 16 to 31 August),
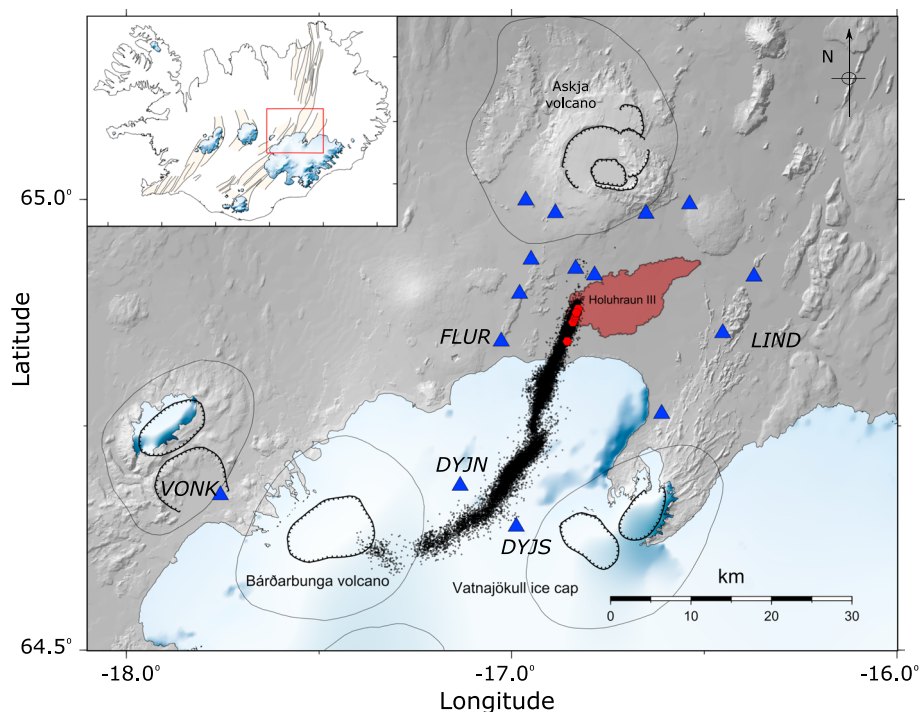
Figure 1. Volcanic setting: Topography in gray with ice cover in white; beige overlays in inset show rift segments (Einarsson & Saemundsson, 1987); earthquake locations trace the dike path (black dots, from Ágústsdóttir et al., 2016); blue triangles are the seismic stations used in this study; red hexagons correspond to the eruptive vents active during the fissure eruption; solid black lines indicate central volcanoes; and inner dashes display calderas. Seismic stations mentioned in the text are labeled.

magma migrated laterally along a dike from the Bárðarbunga volcano, 48 km NE to the eventual eruption site at Holuhraun (Ágústsdóttir et al., 2016, Figure 1). An open pathway was formed after the dike emplacement and magma continued to flow along a conduit with a maximum depth of ~6 km below sea level. The propagation route was controlled by the lithostatic pressure and the stress field of the divergent plate boundary (Heimisson et al., 2015; Sigmundsson et al., 2015). This example showed how tracking of magma migration with seismic signals has significant societal and scientific importance.

The 2 week long dike propagation was traced by using classical seismic techniques (Ágústsdóttir et al., 2016) to detect and locate migrating swarms of earthquakes at the tip of the dike. A local network of more than 70 broadband seismic stations recorded over 30,000 earthquakes which delineated the path of the magma and revealed the fracture mechanisms at the tip of the dike (Ágústsdóttir et al., 2016). The seismicity displayed complex dynamics consisting of advances of the tip of the dike at rates of 0.3 to 4.7 km/h separated by stalled phases lasting up to 81 h (Ágústsdóttir et al., 2016).

A 6 month long eruption started on 31 August 2014, after a minor fissure erupted in Holuhraun that lasted for about 4 h on 29 August (Sigmundsson et al., 2015) and erupted more than $1.5 + -2$ km^3 of lava (Gíslason et al., 2015; Gudmundsson et al., 2016). The magma source is thought to lie beneath Bárðarbunga caldera, which collapsed slowly over the eruption period (Gudmundsson et al., 2016). Three tremor sources with different mechanisms were associated with the eruption (Eibl, Bean, Jónsdottir, et al., 2017), including a source south of the eruption fissure on 3 September (Eibl, Bean, Vogfjörd, et al., 2017).

The aim of this study is to show that an alternative technique based on the radiated seismic energy, rather than discrete earthquake locations, can be used to investigate the migration and eruption of magma. Unlike individual earthquake location procedures, the Seismic Amplitude Ratio Analysis (SARA) does not rely on clear *P* and *S* arrivals to locate a seismic source. While individual earthquake locations identify the position of energetic fracture events, the SARA method resolves the location of the bulk seismic energy, and the often less impulsive processes generated during magma migration, by using the amplitude recorded at different stations (Kanamori, 1993).

The amplitude source location method was originally proposed by Battaglia and Aki (2003) to overcome the limitations of traditional methods to locate earthquakes. It has already been applied successfully to locate various volcano-seismic signals (Battaglia, Aki, & Ferrazzini, 2005; Battaglia, Aki, & Staudacher, 2005; Eibl et al., 2014; Kumagai et al., 2010, 2011, 2013, 2014, 2015; Kurokawa et al., 2016; Ogiso & Yomogida, 2012, 2015; Ogiso et al., 2015) using high-frequency seismic amplitudes and assuming isotropic radiation of S waves. A grid search is usually conducted to find a source location that provides the best fit between observed envelope amplitudes corrected for site amplification factors at individual stations and calculated amplitudes using the far-field S wave equation with isotropic radiation (Morioka et al., 2017). Recent numerical simulations in realistic heterogeneous volcanic structures demonstrated the applicability of the method in highly heterogeneous media with transport mean free paths of 10^3 m or smaller and strong intrinsic attenuation (Morioka et al., 2017). Finally, the method was recently calibrated using active seismic sources showing moderate influence of attenuation and velocity on location but much stronger influence of site amplification factors (Walsh et al., 2017). This novel method is therefore complementary to traditional earthquake location methods and has also been used to reveal magma migration pathways prior to the 2010 Piton de la Fournaise eruption (Taisne et al., 2011) and the 2012-2013 Tolbachik eruptions (Caudron et al., 2015). However, it has never been calibrated and compared with well-resolved earthquake locations using an extended seismic network. Integrating both approaches provides an opportunity to investigate the spatiotemporal characteristics of magma migration during the 2014 Holuhraun dike intrusion and ensuing eruption with remarkable accuracy. It also allows us to study the dynamics of dike inflation and propagation during the rifting event, particularly during stalled phases and during the fissure eruption.

2. Methodology and Data Processing

The SARA methodology computes the ratios of seismic amplitudes recorded at different seismic stations, which are therefore independent of the absolute seismic energy radiated at the source:

$$\frac{A_1}{A_2} = \left(\frac{r_2}{r_1}\right)^n \exp(-B(r_1 - r_2)) \tag{1}$$

with,

$$B = \frac{\pi f}{Q\beta} \tag{2}$$

where A_1, A_2 are the seismic amplitudes at stations 1 and 2, r_1, r_2 are the distances between the source and stations 1 and 2, $n = 1$ for body waves and $n = 0.5$ for surface waves, β is the seismic wave velocity, Q is the Quality Factor for attenuation (for shear waves in this case, see paragraph below), and f is the central frequency. We then seek a spatial location such that the theoretical ratios best fit the observed ones for the set of station pairs (Taisne et al., 2011).

A shear wave velocity was used because S waves dominate the body wave amplitude regime. We make the assumption that the S wave radiation pattern is isotropic at high frequencies (above 1 Hz), particularly for S wave amplitudes (Takemura et al., 2016). This assumption is thought to be valid because scattering due to small-scale heterogeneities leads to homogenization (Battaglia & Aki, 2003; Takemura et al., 2009).

Lower standard deviations in the SARA locations were obtained with Q values below 200, and our tests revealed a better fit with the earthquakes location for Q values above 150 (see section 4.1). A Q value of 175 was therefore chosen to derive the locations. This value concurs with Menke et al. (1995) who found $Q_s = 250$ below 12 km depth and $Q_s = 100$ (where Q_s is the quality factors for shear waves) in the uppermost 4 km of the Icelandic crust. Furthermore, Ólafsson et al. (1998) derived Q varying between 128 and 425 from path-averaged crustal shear wave quality factors. Lateral variations in the attenuation properties appear unlikely considering the small crustal volume affected by the dike propagation, as already suggested by Green et al. (2015).

2.1. Preprocessing and Calculation of Site Amplification Factors

The seismic network has been operated since 2006 and comprised 72 three-component broadband seismometers (6TD 30 s, ESP 60 s, and 3T 120 s of natural period) during the 2014–2015 eruption. The network provides good azimuthal coverage, with excellent sampling north of the ice cap (Ágústsdóttir et al., 2016). All data were recorded at 100 Hz sample rate with a GPS time stamp. The spacing between the stations used in this study is generally around ~10 km but can be as large as 20 km on the ice cap (Figure 1). A maximum
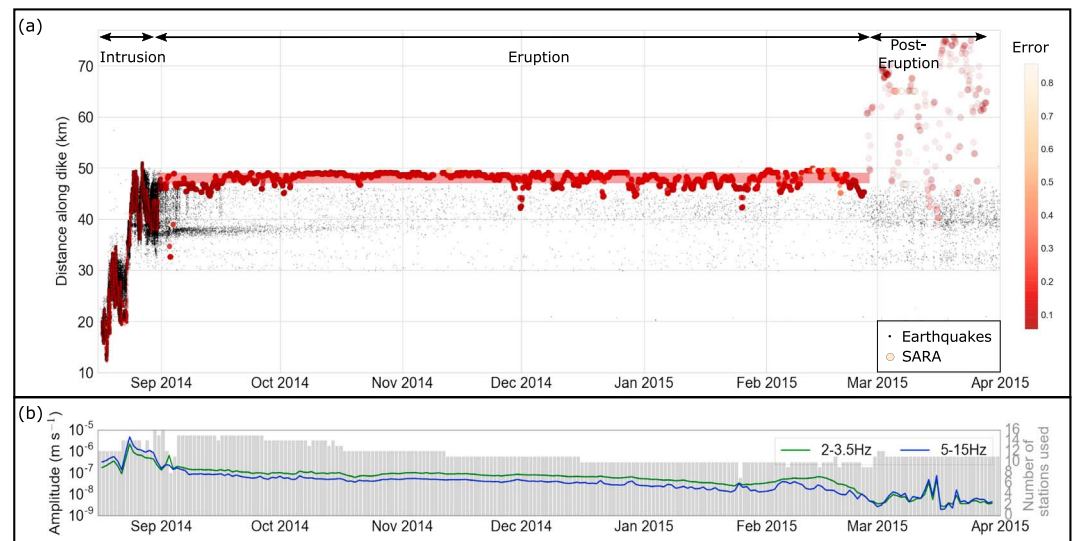
Figure 2. SARA temporal locations: (a) Epicentral location evolution derived using the SARA (method 1 in the 2–16 Hz frequency band). Each circle represents a 30 s location smoothed using a 2 h rolling median window during the intrusion and a 2 h location smoothed using a 6 h rolling median window during the eruption and posteruption. The color of each circle corresponds to the error calculated for an individual location (standard deviation normalized by the maximum value for the period). Earthquake locations (Ágústsdóttir et al., 2016) are shown as black dots. The red shaded area around ~48 km corresponds to the fissure eruption site. (b) Number of stations used (gray bars) and amplitude between 2–3.5 Hz and 5–15 Hz (median per day calculated at station FLUR from the mean absolute amplitude calculated every 30 s).

of 15 stations (Guralp 6TDs and ESPs) was used to derive the locations using the SARA. Stations far from the seismic source (>70 km) adversely affected the results and so were not used. Including more stations near the activity resulted in an increase of computation time, without improving the location accuracy. We used the same seismic network as Ágústsdóttir et al. (2016).

The instrument responses were first removed. We took advantage of the open-source MSNoise software (Lecocq et al., 2014) to scan the archive and define jobs. We then branch to the MSNoise SARA (Seismic Amplitude Ratio Analysis) plugin to process the data. Walsh et al. (2017) showed a strong influence of site amplification factors on the locations. To estimate them, earthquakes with magnitudes larger than 3 and located between 50 and 250 km from the area of interest were selected. The set of earthquakes (19 in total) covered all azimuths, although more earthquakes were located in regions to the north and to the southwest. The site amplification factor estimates followed the procedure described in Kumagai et al. (2010): a band-pass filter was applied, the envelope was computed, and the spectral ratios were calculated in five windows, each of which had a 10 s interval and a 5 s overlap starting from a lapse time that was twice the *S* wave arrival time. The site amplification factors are provided in Table S1 in the supporting information.

The seismic data were subsequently detrended and cosine tapered before being resampled to 40 samples per second because the majority of the energy radiated by volcano-tectonic earthquakes is below 20 Hz (Lahr et al., 1994). The resulting traces were band-pass filtered between 2 and 16 Hz, the frequency band used for earthquake location by Ágústsdóttir et al. (2016). Unless mentioned (see section 4), this frequency band was used to present and discuss the results in this study. Lastly, the envelope of the filtered data was calculated.

2.2. Source Location Methods
Two methods were applied to obtain the SARA locations. The two-dimensional and three-dimensional misfits (Taisne et al., 2011) were computed between the calculated ratios and the theoretical ones (with $Q = 175$, $n = 0.5$, $\beta = 3.5$ km/s and a central frequency of 9 Hz in equation (1)), assuming a homogeneous and isotropic medium. We only calculated 30 s locations during the dike propagation. During the eruption and after we derived a location every 10 min.
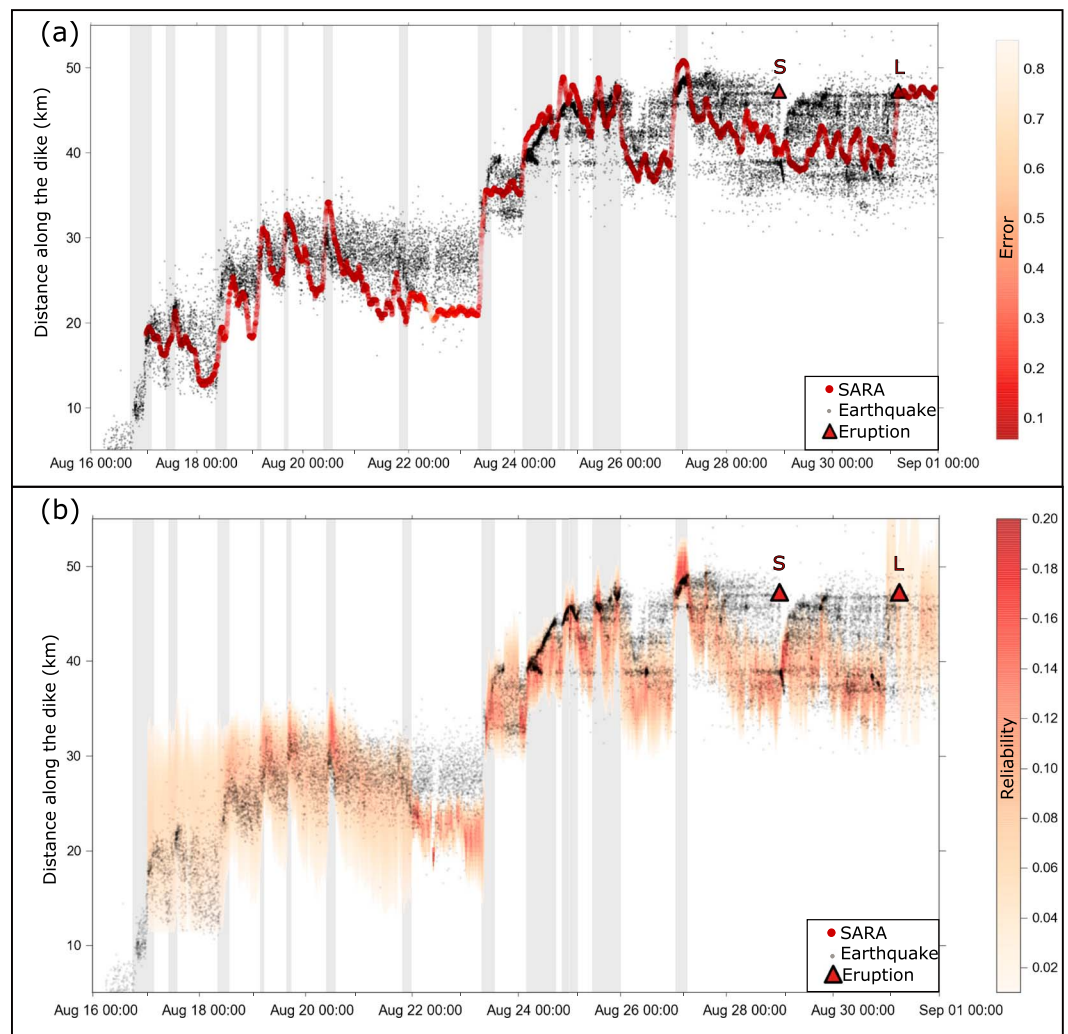
Figure 3. SARA locations during the dike propagation in 2014: (a) Locations derived from method 1 in the 2–16 Hz frequency band. Each circle represents a 30 s location smoothed using a rolling median window of 2 h. The color of each circle corresponds to the error calculated for each 30 s location (standard deviation normalized by the maximum value for the period). The black dots are the earthquakes located by Ágústsdóttir et al. (2016). (b) Locations extracted from the central value of the 1% density curve around the local minimum (method 2, see Figure S1, in the 2–16 Hz frequency band). The color shows the reliability of the estimate (red colors meaning low errors and white colors high errors). For both panels, the gray bands highlight the forward migrations, and the onset of short-lived and 6 month long eruptions are shown as red triangles and labeled S and L, respectively.

2.2.1. Method 1

First, we searched for the value minimizing the misfit in the 2-D and 3-D grids (of 500 m resolution) and computed the standard deviations of the data distributed at 10% around the minimum (Figure 2 with color of the circles: red = low error; white = high error). However, this approach fails if distinct seismic sources radiate seismic energy simultaneously at different locations. To overcome this issue, another technique (Method 2) was explored. The SARA locations during the dike propagation and the eruptions are presented in Tables S2 and S3, respectively.

2.2.2. Method 2

This procedure examined the 2-D misfits in the depth layer of interest (between 0 and 7.5 km in this case). Rather than exporting a single minimum, the program first found the different minima in the image (Figure S1). To assess the reliability of the local minimum, a Gaussian kernel density estimator was implemented. Then 1, 2, and 5% of values around the local minimum were typically extracted (Figure S1). These values were then plotted along with the density of the kernel estimator providing a straightforward way to assess the reliability of the derived location. The derived locations can be found in Table S4.
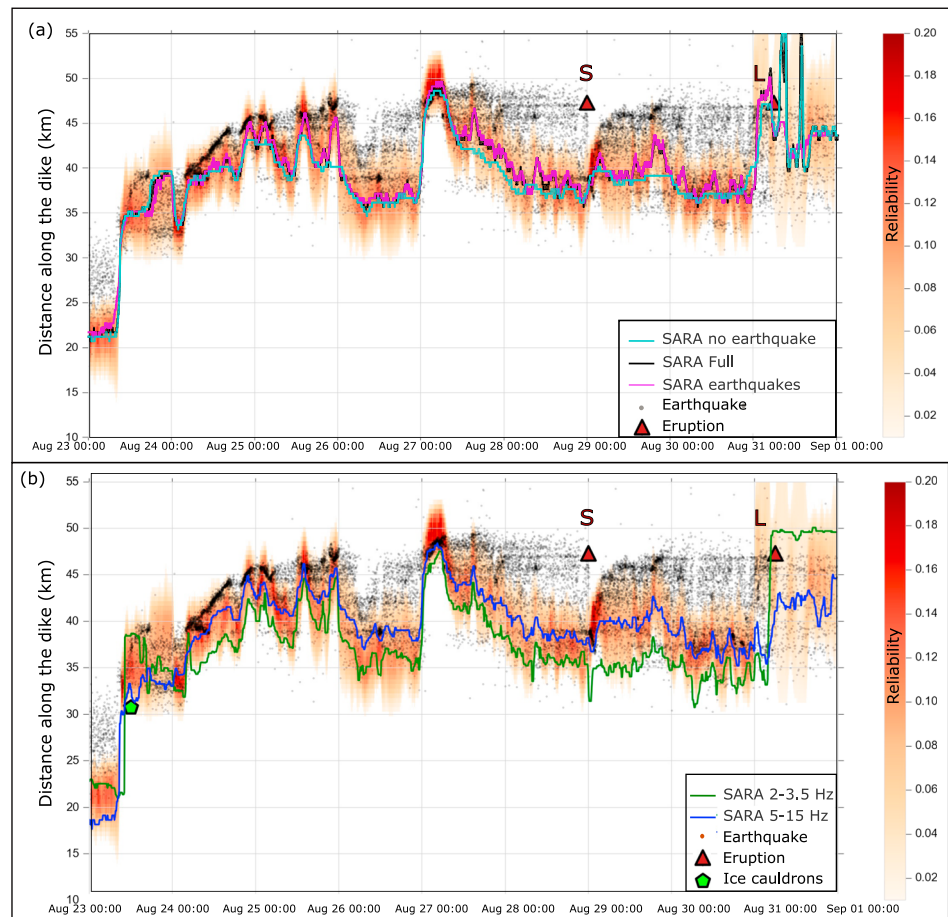
Figure 4. SARA locations during the most intense periods of dike propagation in 2014: Same as Figure 3b but between 23 August and 1 September 2014. (a) The source location (method 2 in the 2–16 Hz frequency band) was computed using SARA measured in time windows when there were no earthquake arrivals (cyan line), and in time windows only around earthquake arrivals (purple line). The black line shows the 2–16 Hz source location which mostly overlaps the purple line. (b) The source location was computed in different frequency bands; 2–3.5 Hz (green) and 5–15 Hz (blue). The low-frequency locations always fall behind the high-frequency line except on 23 and 31 August at the onset of the large fissure eruption. Ice cauldron location and date of formation is from Reynolds et al. (2017). For both panels, short-lived and 6 month long eruptions are shown as red triangles and labeled S and L, respectively.

Preliminary tests (with $n = 1.0$ in equation (1)) located depths dominantly between 5 and 7 km in agreement with the discrete seismic event locations (Ágústsdóttir et al., 2016). However, the choice of Quality factor and frequency variation had too much impact on the depth estimate to reliably estimate the depth in this study.

3. Results

The SARA technique identified the three main phases: dike propagation, eruption, and posteruption (Figure 2). During the dike propagation phase (prior to 1 September 2014), SARA locations corresponded remarkably well to earthquake locations derived from travel time inversion and presented by Ágústsdóttir et al. (2016) (Figures 2 and 3). The SARA technique captured forward propagations and also backward migrations of seismicity and stalled phases following dike advances (Figures 3 and 4a). However, several discrepancies were observed between SARA and earthquake locations. To study this 2 week intrusion in more detail, SARA locations were computed every 30 s. Rolling moving medians and standard deviations of 2 h were used to smooth out individual 30 s locations.

The SARA technique failed on 16 August due to limited network coverage. Between 17 and 20 August, locations derived from method 1 and earthquake locations coincided (Figure 3a). Migrations were more sharply delineated by the SARA methodology. On 21–22 August SARA locations were not in agreement
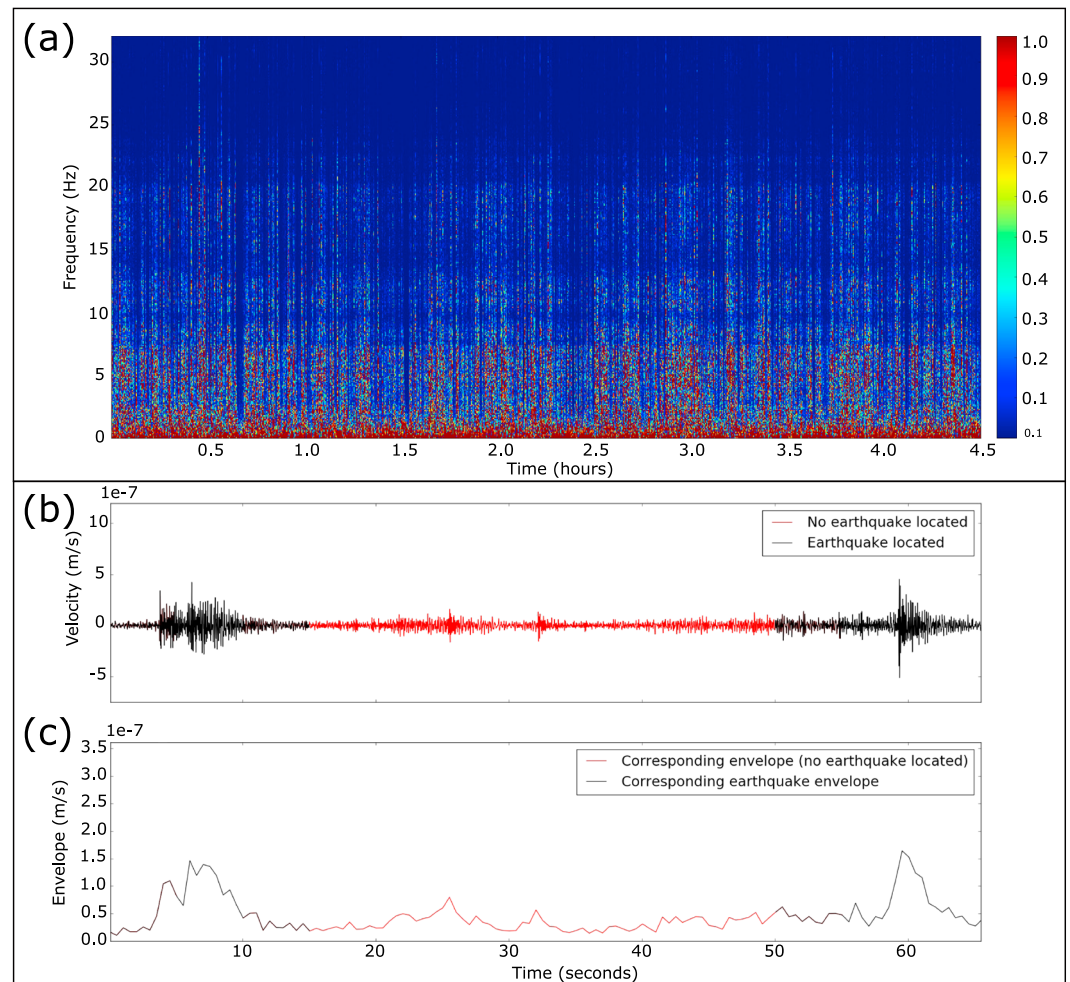
Figure 5. Spectrogram, waveform and envelope example: (a) Normalized amplitude spectrogram (10 s window, not resampled) computed between 01:00 and 05:29 on 23 August at station LIND (see Figure 1 for station location) (b) example of a seismic record (filtered between 2 and 16 Hz) with windows comprising located earthquakes in black and without any located earthquake in red (c) corresponding envelope.

with earthquake hypocenters, which will be discussed later (see section 4.2). Locations extracted from method 2 (Figure 3b) appeared less reliable in the time period 17 to 22 August compared to the most intense phases of seismic activity (after 22 August), most likely due to the absence of stations located nearby the dike (DYJN and DYJS, Figure 1, deployed on 21 August). After 22 August, source locations from method 2 were better resolved due to improved network coverage. We focused on this time period to study in greater detail the dynamics of dike propagation (Figure 4a).

Locations derived from the SARA technique coincided with earthquake locations during surges of events at the tip of the dike (Figure 4a). However, they systematically focused at the back of the active segment during stalled phases, while the earthquakes were mostly radiated along the entire segment over a ∼10−15 km region (e.g., 22−23 August (Figure 3) and 26 August (Figure 4)). These results highlight a preferential release of seismic energy at the back of the active dike segment during stalled periods together with a larger spatial extent of the seismicity.

To assess further the reliability of this methodology with and without the presence of clear earthquakes, source locations were computed in time windows when there were no earthquakes located by Ágústsdóttir et al. (2016) and then in time windows only comprising earthquake arrivals (Figures 5b and 5c). SARA locations containing earthquake arrivals-only and overall results overlap (purple and black lines respectively in Figure 4a). Locations derived by selecting windows without any located earthquakes by Ágústsdóttir et al. (2016) (cyan line Figure 4a) sometimes slightly lag behind. Yet they reveal the existence of seismic energy

located in the absence of discrete brittle failure earthquakes. These small events may have been buried in the high background ambient noise preventing their detection by conventional travel time methods due to their low signal-to-noise ratios.

During the entire eruption, the SARA locations coincided with the main fissure eruption site (Figure 2), except on 3 September. On this date, the SARA location was dominated by another source of seismic energy discussed below (see section 4.2). When the eruption ended on 27 February 2015, SARA locations became scattered abruptly due to the lack of continuous seismic energy (Figure 2).

4. Discussion

General agreement between traditional earthquake locations and SARA locations is obtained during the 2 week long dike propagation (maximum ∼3 km of difference). This section first presents an in-depth assessment of the technical possibilities but also limitations of the SARA methodology. Subsequently, we explore the origin of the continuous seismicity and the reasons for differences observed between SARA locations and discrete earthquake locations during specific time periods.

4.1. Technical Limitations

Uncertainties in SARA locations include the effects of the seismic network, namely, the number of stations and its geometry, as well as uncertainties in attenuation, velocity models, and site amplification factors (Walsh et al., 2017). Although small variations in site amplification factors (±0.5) generally did not impact the source locations, they dramatically influenced the derived locations for isolated stations of this network (e.g., station VONK, Figure 1).

Locations were very similar (<1 km of difference) when removing a given station (Figure 6a). The station VONK appears critical particularly before 23 August 2014 since it covers the entire region close to Bárðarbunga. This is particularly clear on 21 August 2014 (yellow line with triangles, Figure 6a). The removal of FLUR between 11:30 a.m. on 23 August and 2 a.m. on 24 August (purple line, Figure 6a) shifted the locations toward ∼38 km whereas the other curves all remained at ∼32 km distance along the dike. FLUR is the closest station to the ice cauldron that was presumably active on 23 August (see section 4.2). We therefore conclude that only stations installed at critical locations impact the results (i.e., FLUR and VONK).

We then investigated the effect of removing a given number of stations (Figure 6b). Locations remained relatively similar for a maximum number of stations ranging between 9 and 17 (Figure 6c). Our approach based on a nonuniform set of stations determined by a quality assessment appears robust provided the number of stations is sufficiently large.

The Quality Factor-velocity product $Q \times \beta$ is generally poorly constrained in volcanic areas. The temporal evolution for $Q \times \beta$ ranging between 50 and 1,050 (with 1.0 km/s $\leq \beta \leq$ 3.5 km/s and 50 $\leq Q \leq$ 300) was investigated and showed differences in locations (method 1, 10 min data smoothed over 2 h, Figure 7a). Our results showed absolute epicentral locations varying up to ∼5 km for $Q \times \beta$ ranging between 175 and 750 (Figure S3). This observation contrasts with Eibl et al.'s (2014) results at Hekla volcano where they found only slight differences when varying $Q \times \beta$ but with a much smaller aperture network and much shallower seismic events. Results for $Q \times \beta$ below 175 appeared completely unreliable whereas values above 750 located too far along the dike (e.g., Figure 7c) during surges of events at the tip of the dike. Two time periods showed large differences in epicentral locations: before 13:30 18 August and between 23:50 21 August and 08:30 23 August. These periods coincided with lower radiation of seismic energy (Figure 7b). These results highlight the need to carefully estimate $Q \times \beta$ and site amplification factors to retrieve robust locations using SARA.

In terms of resolution, the following example highlights the limited capability of the SARA methodology to discriminate between closely spaced sources. On ∼02:00 24 August, two branches of earthquakes, less than 4 km apart, propagated simultaneously during a few hours (Figure 4a). SARA locations were sensitive to the strongest seismic source, i.e., the branch that slightly retreated along the dike, rather than the branch propagating forward along the dike.

4.2. Nature of the Seismicity

Excellent agreement was reached between (1) micro-earthquake and SARA locations during dike propagation, except on 23 and 24 August and (2) the eruption site and SARA locations during the 6 month long eruption (generally less than 3 km difference), except on 3 September. The results presented in Figures 2–4
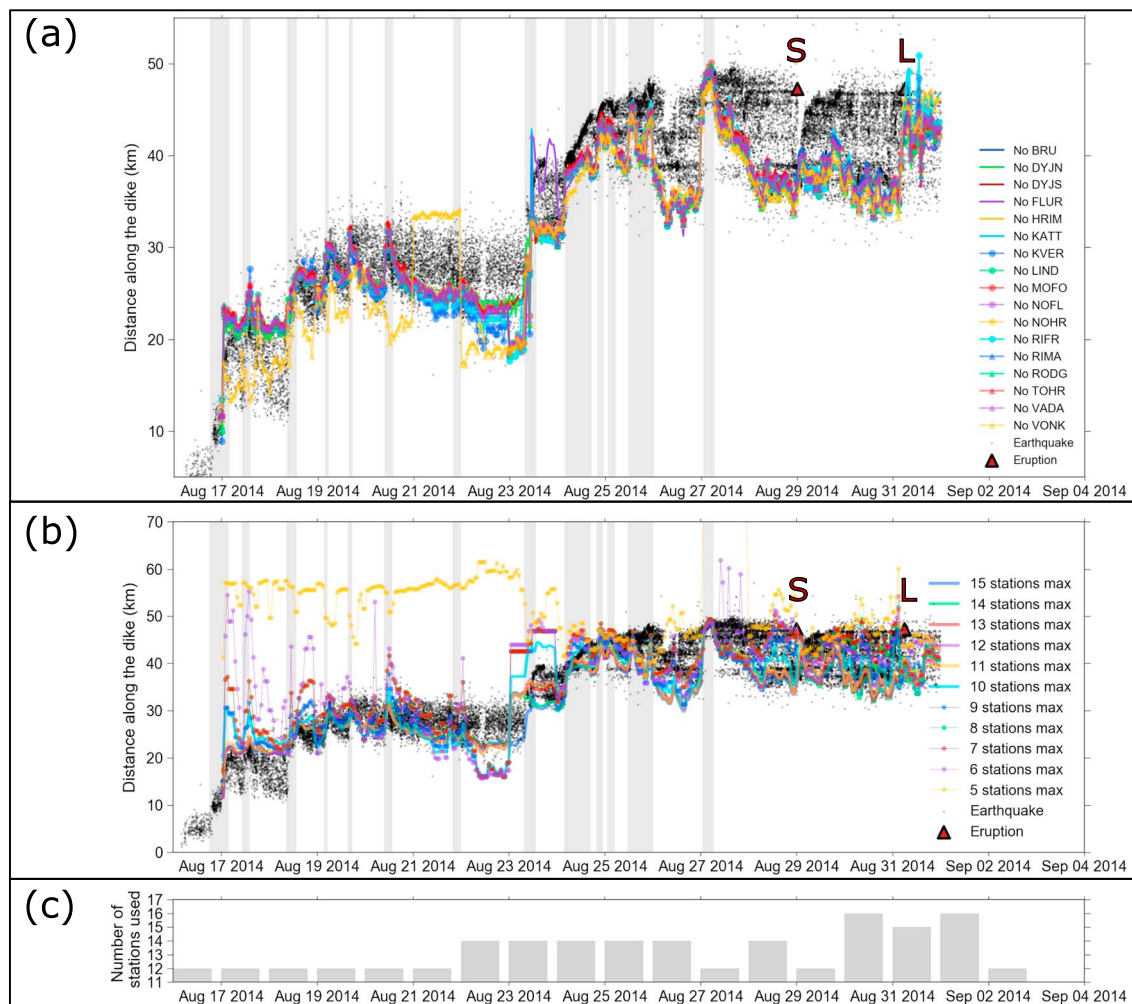
Figure 6. Time evolution of SARA locations during the dike propagation depending on the seismic network: (a) SARA locations derived from method 1 (2–16 Hz frequency band). Each point corresponds to a 10 min location smoothed using a rolling median window of 2 h. Each color corresponds to a station removed during the location procedure. (b) SARA locations derived from method 1 (2–16 Hz frequency band). Each point corresponds to a 10 min location smoothed using a rolling median window of 2 h. Each color corresponds to the maximum number of stations available during the location procedure. The stations were gradually removed in alphabetical order, from 15 to 5. (c) Number of stations used (gray bars). For Figures 6a and 6b, the gray bands highlight the forward migrations, and the onset of short-lived and 6 month long eruptions are shown as red triangles and labeled S and L, respectively.

were obtained for data filtered between 2 and 16 Hz. During the dike intrusion the energy was predominantly radiated in the 5–15 Hz band (Figure 5a), whereas during the eruption it focused between 2.0 and 3.5 Hz (Figure 2). Locations using different frequency bands are explored for each time period to isolate possibly distinct source processes. The potential sources triggering this seismicity during the dike intrusion are first discussed, followed by the discussion of periods during which discrepancies were found. We follow the same scheme for the eruption.

4.2.1. Dike Intrusion

During dike propagation, the SARA and earthquake epicentral locations agreed. The SARA technique highlighted the continuous radiation of seismic energy, even in the absence of located earthquakes. These time periods were characterized by tiny seismic events. This finding is in line with results obtained by Bakker et al. (2016) using dike injection experiments, who showed that the seismicity not only peaks during initial fracturing but persists while the pressure decreases and the dike stalls.

During the most vigorous seismic activity, SARA locations at low frequencies (2.0–3.5 Hz) consistently lagged behind the high-frequency locations (5–15 Hz, Figure 4b). We restrict our analysis to the high frequencies (>2 Hz) as defined by Takemura et al. (2009), where the S wave radiation pattern becomes rapidly isotropic
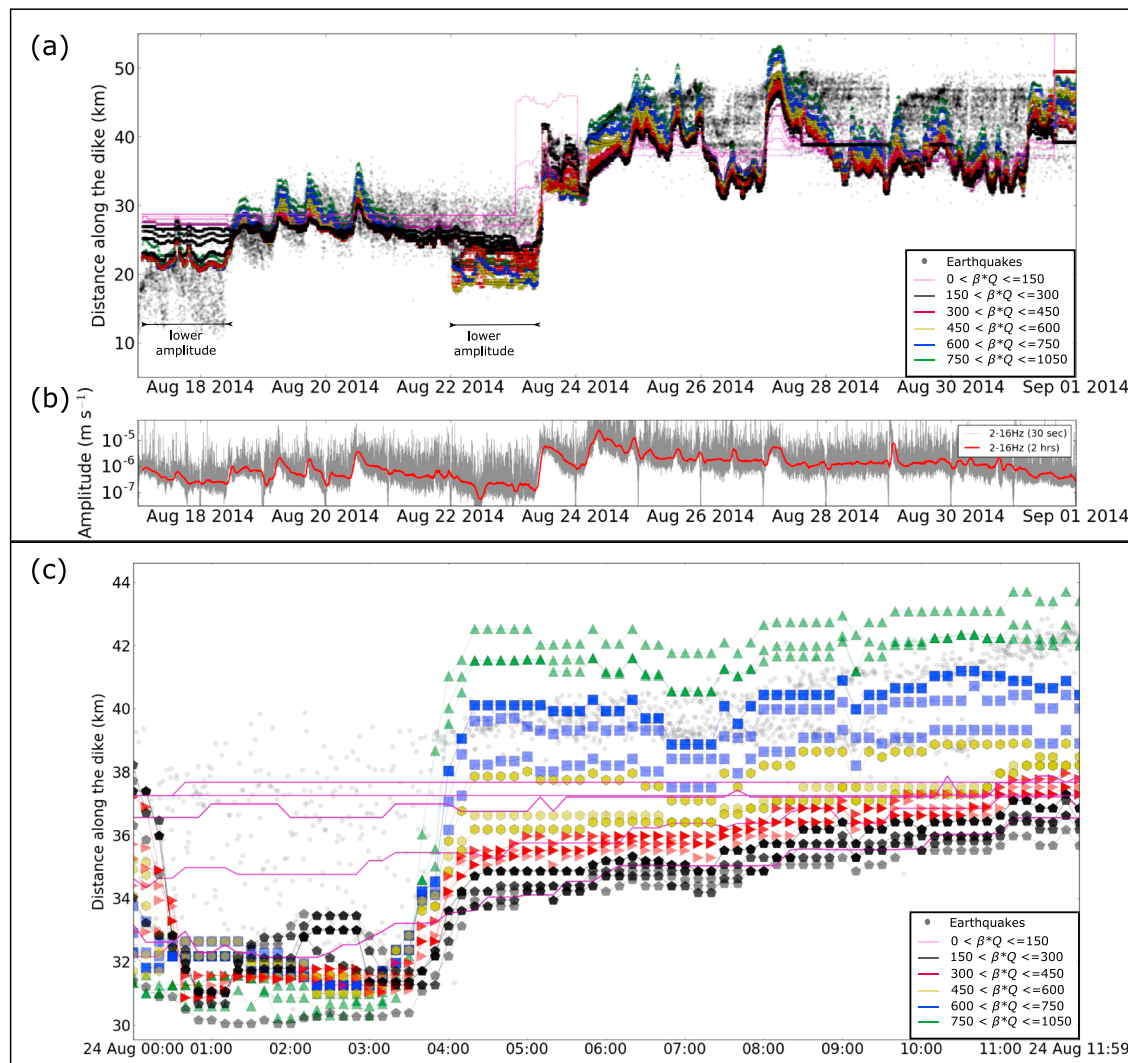
Figure 7. Time evolution of SARA locations during the dike propagation depending on the **Q × β** product: (a) SARA locations derived from method 1 (2–16 Hz frequency band). Each point corresponds to a 10 min location smoothed using a rolling median window of 2 h. Each color corresponds to a range of $Q \times \beta$ product. The black dots are the earthquakes located by Ágústsdóttir et al. (2016). (b) Temporal evolution of the seismic amplitude filtered between 2 and 16 Hz (station FLUR). The 30 s and 2 h values are plotted in gray and red, respectively. (c) Zoom on 24 August between 00:00 and 12:00 a.m. showing the SARA locations evolution as a function of $Q \times \beta$ products. The duplicated $Q \times \beta$ products appear darker (e.g., 600 and 750).

away from the source. This assumption holds for large source-station distances as observed in this study (Figure 1). Notably, the locations using different frequencies were in better agreement during propagations at the tip of the dike but could be up to 5 km apart during dike stalling. High-frequency brittle failure probably continuously occurred at the tip of the dike as it propagated, while dike inflation continuously generated lower-frequency seismicity further back behind the dike tip. An exception was observed on 23 August when the higher frequency locations focused behind the lower-frequency locations. This time period included some of the strongest tremor, and ice cauldrons were observed at the surface in the same vicinity a few days later (Eibl, Bean, Vogfjörd, et al., 2017; Reynolds et al., 2017). This swap between low- and high-frequency locations was the only observation of this kind during the dike intrusion and might be related to a subglacial eruption. An in-depth investigation of this low-frequency sequence is the topic of an ongoing study.

Another puzzling and consistent observation concerned backward migration and stalling phases directly following forward migrations. This particular stalling pattern had previously been observed, although less clearly, for example, during the 17 June 2006 rifting episode in the Afar (Ethiopia) (Rivalta et al., 2015), and during the 2000 Miyakejima (Japan) dike intrusion (Uhira et al., 2005). During the Bárðarbunga-Holuhraun rifting event, the microseismicity was radiated over a ~10–15 km region (Figures 3 and 4, as previously shown
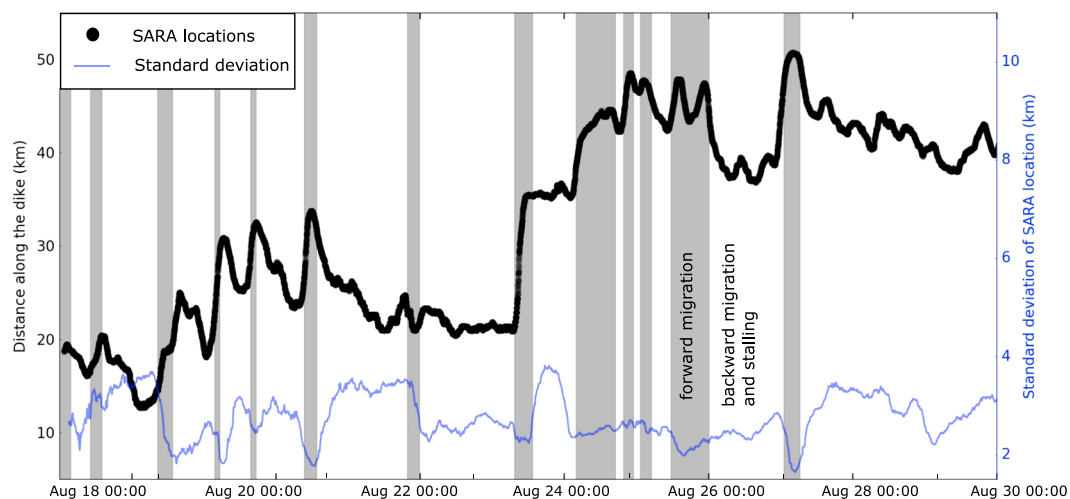
Figure 8. Dike stalling and spatial extent of the seismicity: SARA locations (black line, method 2 in the 2–16 Hz frequency band) and their standard deviation (blue line) showing the spatial extent of the seismic energy source. Minimum standard deviation (i.e., small extent of seismic activity) is observed during propagation phases, maximum during the stalled phases. The gray bands correspond to forward migrations.

by Ágústsdóttir et al., 2016), while SARA locations were focused at the back of the active segment. This consistent observation appears as a robust feature since the SARA locations were reliable (Figure 3b).

Another intriguing feature is that the seismic energy source has a systematically larger spatial extent during these stalled periods (up to 4 km, blue line in Figure 8), as shown by the larger standard deviation of the 30 s SARA locations (smoothed using a 6 h rolling median). This pattern could be simply due to inflation of the dike segment, activating larger areas of seismic activity. Another explanation is that dike deceleration and stalling led to a change in the dike's shape, as proposed previously based on propagation models of fluid-filled cracks (Dahm et al., 2010). This could explain why the seismic energy was released preferentially at the back of the dike.

4.2.2. Eruption

The SARA technique also showed that there was radiation of seismic energy that was steadily focused around the magma discharge site during the entire 6 month long eruption (Figure 2). The energy captured during the eruption seemed primarily associated with the magma emission site, similar to the 2010 Piton de la Fournaise and 2012–2013 Tolbachik eruptions (Taisne et al., 2011, and Caudron et al., 2015, respectively). The majority of the energy was released at lower frequency (<3.5 Hz, Figure 2). High-frequency locations (5–15 Hz) were likely to consist of a mixture between eruptive and micro-earthquake sources since they were mostly focused around ∼45 km (Figure S4). SARA locations became completely unreliable after the end of the eruption due to the lack of seismic energy.

The only exception occurred on 3 September when SARA locations focused close to the ice cauldrons (∼35 km, Figure 2). Eibl, Bean, Vogfjörd, et al. (2017) located tremor on 3 September 2014 using seismic array processing techniques and reported locations in the vicinity of ice cauldrons. They ascribed it to swarms of microseismic events during dike formation associated with fracturing of the upper 2–3 km of the crust and preceding sub-glacial eruptions. The results presented in this study could not confirm this hypothesis, although the SARA location was dominated by a source at a similar location.

5. Conclusion

The 2014–15 Bárðarbunga-Holuhraun dike intrusion and eruption was one of the best monitored dike injections globally due to a dense network of seismometers. This study explores the seismic data set to assess the capabilities of the SARA methodology to locate seismicity reliably. During the 2 week long dike propagation, SARA locations overall were remarkably consistent with the >30,000 seismic events located by Ágústsdóttir et al. (2016), although several discrepancies were observed. The SARA technique continuously detected and located seismic energy, even in the absence of located earthquakes. A systematic retreat and stalling to the back of the active segment was clearly observed during the stalled phases. A larger spatial extent of the

seismic energy source was activated during these periods. This pattern of seismicity could be explained by dike inflation and/or by the dike's shape. Low-frequency (2.0–3.5 Hz) locations focused around ice cauldrons on 23 August possibly associated with subglacial eruptions, but a dedicated study is required to properly investigate this feature. The SARA locations were then focused around the eruptive site for 6 months (Figure 2), except on 3 September when tremor was observed near ice cauldrons farther south. From a technical perspective, we recommend using a kernel density estimation to assess the reliability of the results, and robust site amplification, $Q \times \beta$ estimates to avoid serious mislocations. Closely spaced sources (less than 4 km) could not be isolated with this seismic network.

The method is an appealing tool for volcano-seismologists as it can be applied in volcanic settings where the seismic networks are sparse or the intrusion/eruption simply does not generate clear distinct microseismic events. Tracking the magma migration in these circumstances is valuable, and this study provides the first robust validation of the SARA method, because source locations could be compared with the high-quality earthquake data set for an integrated interpretation of the seismic data.

References

Ágústsdóttir, T., Woods, J., Greenfield, T., Green, R. G., White, R. S., Winder, T., . . . Soosalu, H. (2016). Strike-slip faulting during the 2014 Bárðarbunga-Holuhraun dike intrusion, central Iceland. *Geophysical Research Letters*, *43*, 1495–1503. https://doi.org/10.1002/2015GL067423

Bakker, R. R., Fazio, M., Benson, P. M., Hess, K.-U., & Dingwell, D. B. (2016). The propagation and seismicity of dyke injection, new experimental evidence. *Geophysical Research Letters*, *43*, 1876–1883. https://doi.org/10.1002/2015GL066852

Battaglia, J., & Aki, K. (2003). Location of seismic events and eruptive fissures on the Piton de la Fournaise volcano using seismic amplitudes. *Journal of Geophysical Research*, *108*(B8), 2364. https://doi.org/10.1029/2002JB002193

Battaglia, J., Aki, K., & Ferrazzini, V. (2005). Location of tremor sources and estimation of lava output using tremor source amplitude on the Piton de la Fournaise volcano: 1. Location of tremor sources. *Journal of Volcanology and Geothermal Research*, *147*(3), 268–290. https://doi.org/10.1016/j.jvolgeores.2005.04.005

Battaglia, J., Aki, K., & Staudacher, T. (2005). Location of tremor sources and estimation of lava output using tremor source amplitude on the Piton de la Fournaise volcano: 2. Estimation of lava output. *Journal of Volcanology and Geothermal Research*, *147*(3), 291–308. https://doi.org/10.1016/j.jvolgeores.2005.04.006

Caudron, C., Taisne, B., Kugaenko, Y., & Saltykov, V. (2015). Magma migration at the onset of the 2012–13 Tolbachik eruption revealed by Seismic Amplitude Ratio Analysis. *Journal of Volcanology and Geothermal Research*, *307*, 60–67. https://doi.org/10.1016/j.jvolgeores.2015.09.010

Dahm, T., Hainzl, S., & Fischer, T. (2010). Bidirectional and unidirectional fracture growth during hydrofracturing: Role of driving stress gradients. *Journal of Geophysical Research*, *115*, B12322. https://doi.org/10.1029/2009JB006817

Eibl, E., Bean, C. J., Jónsdottir, I., Höskuldsson, A., Thordarson, T., Coppola, D., . . . Walter, T. R. (2017). Multiple coincident eruptive seismic tremor sources during the 2014–2015 eruption at Holuhraun, Iceland. *Journal of Geophysical Research: Solid Earth*, *122*, 2972–2987. https://doi.org/10.1002/2016JB013892

Eibl, E., Bean, C. J., Vogfjörd, K., & Braiden, A. (2014). Persistent shallow background microseismicity on Hekla volcano, Iceland: A potential monitoring tool. *Journal of Volcanology and Geothermal Research*, *289*, 224–237. https://doi.org/10.1016/j.jvolgeores.2014.11.004

Eibl, E., Bean, C. J., Vogfjörd, K. S., Ying, Y., Lokmer, I., Möllhoff, M., . . . O'Brien, G. S. (2017). Tremor-rich shallow dyke formation followed by silent magma flow at Bárðarbunga in Iceland. *Nature Geoscience*, *10*(4), 299–304. https://doi.org/10.1038/ngeo2906

Einarsson, P., & Saemundsson, K. (1987). Íhlutarins eðli, in festschrift for th. sigurgeirsson (geological map). In T. Sigfússon (Ed.), *Íhlutarins eðli, in Festschrift for Th. Sigurgeirsson*. Reykjavík: Menningarsjóður.

Gíslason, S., Stefánsdóttir, G., Pfeffer, M., Barsotti, S., Jóhannsson, T., Galeczka, I., . . . Gudmundsson, M. T. (2015). Environmental pressure from the 2014–15 eruption of the Bárðarbunga volcano, Iceland. *Geochemical Perspectives Letters*, *1*, 84–93.

Green, R. G., Greenfield, T., & White, R. S. (2015). Triggered earthquakes suppressed by an evolving stress shadow from a propagating dyke. *Nature Geoscience*, *8*(8), 629–632. https://doi.org/10.1038/ngeo2491

Gudmundsson, M. T., Jónsdóttir, K., Hooper, A., Holohan, E. P., Halldórsson, S. A., Ófeigsson, B. G., . . . Aiuppa, A. (2016). Gradual caldera collapse at Bárðarbunga volcano, Iceland, regulated by lateral magma outflow. *Science*, *353*(6296), AAF8988. https://doi.org/10.1126/science.aaf8988

Heimisson, E. R., Hooper, A., & Sigmundsson, F. (2015). Forecasting the path of a laterally propagating dike. *Journal of Geophysical Research: Solid Earth*, *120*, 8774–8792. https://doi.org/10.1002/2015JB012402

Hunter, J. D. (2007). Matplotlib: A 2D graphics environment. *Computing In Science and Engineering*, *9*(3), 90–95. https://doi.org/10.1109/MCSE.2007.55

Kanamori, H. (1993). Locating earthquakes with amplitude: Application to real-time seismology. *Bulletin of the Seismological Society of America*, *83*(1), 264–268.

Krischer, L., Megies, T., Barsch, R., Beyreuther, M., Lecocq, T., Caudron, C., & Wassermann, J. (2015). ObsPy: A bridge for seismology into the scientific Python ecosystem. *Computational Science and Discovery*, *8*(1), 014003.

Kumagai, H., Lacson, R., Maeda, Y., Figueroa, M. S., & Yamashina, T. (2014). Shallow *S* wave attenuation and actively degassing magma beneath Taal Volcano, Philippines. *Geophysical Research Letters*, *41*, 6681–6688. https://doi.org/10.1002/2014GL061193

Kumagai, H., Lacson, R., Maeda, Y., Figueroa, M. S., Yamashina, T., Ruiz, M., . . . Yepes, H. (2013). Source amplitudes of volcano-seismic signals determined by the amplitude source location method as a quantitative measure of event size. *Journal of Volcanology and Geothermal Research*, *257*, 57–71. https://doi.org/10.1016/j.jvolgeores.2013.03.002

Kumagai, H., Mothes, P., Ruiz, M., & Maeda, Y. (2015). An approach to source characterization of tremor signals associated with eruptions and lahars. *Earth, Planets and Space*, *67*(1), 178. https://doi.org/10.1186/s40623-015-0349-1

Kumagai, H., Nakano, M., Maeda, T., Yepes, H., Palacios, P., Ruiz, M., . . . Yamashima, T. (2010). Broadband seismic monitoring of active volcanoes using deterministic and stochastic approaches. *Journal of Geophysical Research*, *115*, B08303. https://doi.org/10.1029/2009JB006889

Kumagai, H., Placios, P., Ruiz, M., Yepes, H., & Kozono, T. (2011). Ascending seismic source during an explosive eruption at Tungurahua volcano, Ecuador. *Geophysical Research Letters*, *38*, L01306. https://doi.org/10.1029/2010GL045944

Kurokawa, A., Takeo, M., & Kurita, K. (2016). Two types of volcanic tremor changed with eruption style during 1986 Izu-Oshima eruption. *Journal of Geophysical Research: Solid Earth*, *121*, 2727–2736. https://doi.org/10.1002/2015JB012500

Lahr, J., Chouet, B., Stephens, C., Power, J., & Page, R. (1994). Earthquake classification, location, and error analysis in a volcanic environment: Implications for the magmatic system of the 1989–1990 eruptions at Redoubt Volcano, Alaska. *Journal of Volcanology and Geothermal Research*, *62*(1), 137–151. https://doi.org/10.1016/0377-0273(94)90031-0

Lecocq, T., Caudron, C., & Brenguier, F. (2014). MSNoise, a Python package for monitoring seismic velocity changes using ambient seismic noise. *Seismological Research Letters*, *85*(3), 715–726. https://doi.org/10.1785/0220130073

Menke, W., Levin, V., & Sethi, R. (1995). Seismic attenuation in the crust at the mid-Atlantic plate boundary in south-west Iceland. *Geophysical Journal International*, *122*(1), 175–182. https://doi.org/10.1111/j.1365-246X. 1995.tb03545.x

Morioka, H., Kumagai, H., & Maeda, T. (2017). Theoretical basis of the amplitude source location method for volcano-seismic signals. *Journal of Geophysical Research: Solid Earth*, *122*, 6538–6551. https://doi.org/10.1002/2017JB013997

Ogiso, M., Matsubayashi, H., & Yamamoto, T. (2015). Descent of tremor source locations before the 2014 phreatic eruption of ontake volcano, Japan. *Earth, Planets and Space*, *67*(1), 206. https://doi.org/10.1186/s40623-015-0376-y

Ogiso, M., & Yomogida, K. (2012). Migration of tremor locations before the 2008 eruption of Meakandake Volcano, Hokkaido, Japan. *Journal of Volcanology and Geothermal Research*, *217*, 8–20. https://doi.org/10.1016/j.jvolgeores. 2011.12.005

Ogiso, M., & Yomogida, K. (2015). Estimation of locations and migration of debris flows on Izu-Oshima Island, Japan, on 16 October 2013 by the distribution of high frequency seismic amplitudes. *Journal of Volcanology and Geothermal Research*, *298*, 15–26. https://doi.org/10.1016/j.jvolgeores.2015.03.015

Ólafsson, S., Sigbjörnsson, R., & Einarsson, P. (1998). Estimation of source parameters and Q from acceleration recorded in the Vatnafjöll Earthquake in South Iceland. *Bulletin of the Seismological Society of America*, *88*(2), 556–563.

Reynolds, H. I., Gudmundsson, M. T., Högnadóttir, T., Magnússon, E., & Pálsson, F. (2017). Subglacial volcanic activity above a lateral dyke path during the 2014–2015 Bárdarbunga-Holuhraun rifting episode, Iceland. *Bulletin of Volcanology*, *79*(6), 38. https://doi.org/10.1007/s0044

Rivalta, E., Taisne, B., Bunger, A., & Katz, R. (2015). A review of mechanical models of dike propagation: Schools of thought, results and future directions. *Tectonophysics*, *638*, 1–42. https://doi.org/10.1016/j.tecto.2014.10.003

Sigmundsson, F., Hooper, A., Hreinsdóttir, S., Vogfjörd, K. S., Ófeigsson, B. G., Heimisson, E. R., . . . Eva, P. S. (2015). Segmented lateral dyke growth in a rifting event at Bárðarbunga volcanic system, Iceland. *Nature*, *517*(7533), 191–195. https://doi.org/10.1038/nature14111

Taisne, B., Brenguier, F., Shapiro, N., & Ferrazzini, V. (2011). Imaging the dynamics of magma propagation using radiated seismic intensity. *Geophysical Research Letters*, *38*, L04304. https://doi.org/10.1029/2010GL046068

Takemura, S., Furumura, T., & Saito, T. (2009). Distortion of the apparent *S*-wave radiation pattern in the high-frequency wavefield: Tottori-Ken Seibu, Japan, earthquake of 2000. *Geophysical Journal International*, *178*(2), 950–961. https://doi.org/10.1111/j.1365-246X.2009.04210.x

Takemura, S., Kobayashi, M., & Yoshimoto, K. (2016). Prediction of maximum *P*- and *S*-wave amplitude distributions incorporating frequency-and distance-dependent characteristics of the observed apparent radiation patterns. *Earth, Planets and Space*, *68*(1), 166. https://doi.org/10.1186/s40623-016-0544-8

Uhira, K., Baba, T., Mori, H., Katayama, H., & Hamada, N. (2005). Earthquake swarms preceding the 2000 eruption of Miyakejima volcano, Japan. *Bulletin of Volcanology*, *67*(3), 219–230. https://doi.org/10.1007/s00445-004-0405-3

van der Walt, S., Schönberger, J. L., Nunez-Iglesias, J., Boulogne, F., Warner, J. D., Yager, N., . . . Yu, T. A. (2014). Scikit-image: Image processing in python. *PeerJ*, *2*, E453. https://doi.org/10.7717/peerj.453

Walsh, B., Jolly, A. D., & Procter, J. (2017). Calibrating the amplitude source location (ASL) method by using active seismic sources: An example from Te Maari volcano, Tongariro National Park, New Zealand. *Geophysical Research Letters*, *44*, 3591–3599. https://doi.org/10.1002/2017GL073000